Lord, O. T., Vocadlo, L., Wood, I. G., Dobson, D. P., Clark, S. M., & Walter, M. J. (2012). High-pressure phase transitions and equations of state in NiSi. II. Experimental results. Journal of Applied Crystallography, 45, 726-737. 10.1107/S0021889812016809

manuscript ks5299 for review

Journal of
Applied
Crystallography
ISSN 0021-8898
Editor: **Anke R. Kaysser-Pyzalla**

High-pressure phase transitions and equations of state in NiSi II: Experimental results

Oliver T. Lord*, Lidunka Vocadlo, Ian G. Wood, David P. Dobson, Simon M. Clark and Michael J. Walter

Category: *research papers*

Co-editor:

Professor G. Kostorz

ETH Zurich, Wolfgang-Pauli-Str. 16, CH-8093 Zurich, Switzerland

Telephone: 41 44 633 33 99

Fax: 41 44 633 11 05

Email: gk-iucr@ethz.ch

Contact author:

Oliver Thomas Lord

Department of Earth Sciences, University College London, Gower Street, London, Bristol & Avon, WC1E 6BT, United Kingdom

Telephone: ?

Fax: ?

Email: oliver.lord@bristol.ac.uk

High-pressure phase transitions and equations of state in NiSi II: Experimental results

Oliver T. Lord[a,]*, Lidunka Vočadlo[a], Ian G. Wood[a], David P. Dobson[a], Simon M. Clark[b], Michael J. Walter[c]

[a]*Department of Earth Sciences, University College London, Gower Street, London, WC1E 6BT, UK*

[b]*Advanced Light Source, Lawrence Berkeley National Lab., MS6R2100, 1 Cyclotron Road, Berkeley, CA 94720-8226, USA*

[c]*School of Earth Sciences, University of Bristol, Wills Memorial Building, Queen's Road, Bristol, BS8 1RJ, UK*

*Corresponding Author

Email: O.Lord@ucl.ac.uk

Phone: +44 117 9545421

Fax: +44 117 9253385

Total number of words in Main text: 8456

Abstract: 284

Number of tables: 2

Number of figures: 5

References: 51

Abstract

The high-pressure structures of nickel monosilicide (NiSi) have been investigated to 124 GPa by synchrotron based X-ray powder diffraction studies of quenched samples from laser-heated diamond anvil cell experiments and the equations of state of three of these phases have been determined at room-temperature. NiSi transforms from the MnP (B31) structure (space group *Pnma*) to the ε-FeSi (B20) structure (space group $P2_13$) at 12.5±4.5 GPa and 1550±150 K; upon further compression the CsCl (B2) structure (space group *Pm3m*) becomes stable at 46±3 GPa and 1900±150 K. Thus NiSi will be in the B2 structure throughout the majority of Earth's mantle and its entire core, and will likely form a solid solution with FeSi, which is already known to undergo a B20-B2 transition at high pressure. Data from the quenched (room temperature) samples of all three phases have been fitted to the 3rd order Birch-Murnaghan equation of state. For the MnP (B31) structure this yields K_0 = 165±3 GPa with K_0' fixed at 4 and V_0 fixed at 12.1499 Å^3 atom^{-1} (V_0 from unpublished neutron diffraction measurements on the same batch of starting material; Wood, 2011, Pers. Comm.); for the ε-FeSi (B20) structure K_0 = 161±3 GPa, K_0' = 5.6±0.4 with V_0 fixed at 11.4289 Å^3 atom^{-1}; for the CsCl (B2) structure K_0 = 210±9 GPa, K_0' = 4.6±0.1 and V_0 = 11.09±0.05 Å^3 atom^{-1}. The ambient volume of NiSi, therefore, decreases by 6% at the first phase transition and then by a further 3% at the transition to the CsCl structure. Traces of additional NiSi structures predicted by Vočadlo, Wood and Dobson [(2012). *J. Appl. Cryst*. **45**, in press, ks5298], and labelled therein as *Pbma*-I, *Pnma*-II, *Pnma*-III and possibly also *P4/nmm* have been detected.

Keywords: *NiSi, nickel silicide, diamond anvil cell, equations of state, high-pressure, Earth's core*

Synopsis: The high pressure structures of NiSi and their room temperature equations of state have been investigated using synchrotron X-ray diffraction in a diamond anvil cell coupled with laser

annealing. An ε-FeSi-structured phase was found to form above ~13 GPa and a CsCl-structured phase above ~61 GPa.

1. Introduction

Nickel silicide (NiSi) is an intermetallic compound which crystallises in the MnP (B31) structure (space group: *Pnma*) at ambient conditions with $a \sim 5.18$ Å, $b \sim 3.33$ Å, $c \sim 5.61$ Å, $Z = 8$ and $V_0 \sim 12.10$ Å^3 atom^{-1} (Toman, 1951). Due to its utility as a contact material in electronic devices and its possible presence as an impurity in silicon based electronics, this material has been studied extensively at ambient conditions with respect to its structural, electronic, vibrational, elastic and thermal properties (e.g.: Connétable & Thomas, 2009; Acker *et al*., 1999). NiSi has also been studied at high temperatures, where it exhibits the unusual property of highly anisotropic thermal expansion, whereby the *b*-axis contracts as the temperature is raised (Wilson & Cavin, 1992; Rhabadanov & Ataev, 2002a; 2002b; Detavernier *et al*., 2003). As yet, however, this material has not been studied experimentally at high pressures, probably because such studies have no obvious utility to the electronics industry.

The high-pressure behaviour of NiSi is, however, of interest to geophysicists because both elements within the compound are expected to be present within the Earth's core. Geochemical models based on cosmochemical arguments (e.g.: Allègre *et al*., 1995) suggest that the bulk core (i.e.: the solid inner core and liquid outer core combined) could contain at least 5 wt% nickel and 7 wt% silicon (in combination with other light elements such as C, S, O and H). As a result, many studies have been published which focus on various aspects of binary and ternary alloys within the Fe-Ni-Si system, including their phase relations (Lin *et al.*, 2002; Mao *et al.*, 2006; Asanuma *et al*., 2008; Kuwayama *et al*., 2008; 2009; Sakai *et al*., 2011), melting behaviour (e.g.: Morard *et al*., 2011), equations of state (e.g.: Lin *et al*., 2003a; Asanuma *et al*., 2011) and sound velocities (e.g.: Badro *et al*., 2007; Lin *et al.*, 2003b). While the majority of these studies focus on alloy compositions toward the iron-rich corner of the Fe-Ni-Si ternary, studying the high-pressure behaviour of end-member compounds, such as NiSi, is also of great utility in spite of the fact that they are unlikely to be present as pure phases within the Earth.

Here, the primary motivation for studying NiSi is to better understand both the solid inner and liquid outer regions of the Earth's core. Candidate inner and outer core alloys can be described within a multi-component system of which NiSi forms one of many end-member components. Thermodynamic models of core liquids within this system can then be derived from the known physical properties of the solid end-member compounds. Using this method, models of liquids in the Fe-O-S system have successfully been used to constrain the chemical and physical state of the core (e.g.: Helffrich, 2011; Helffrich & Kaneshima, 2004; 2010). To extend these models to include additional elements, such as nickel and silicon, knowledge of the physical properties (specifically the crystal structure, equation of state and melting curve) of the end-member compounds within the extended Fe-Ni-Si-O-S system are needed.

As described in detail in a preceding paper (Vočadlo *et al*., 2012), an additional motivation for the study of NiSi is to allow comparison of the phase diagram and physical properties of this material with those of FeSi, which, unlike NiSi, has been the subject of several recent high-pressure studies, both experimental (Lord *et al*., 2010; Dobson *et al.*, 2002; 2003) and theoretical (Caracas & Wentzcovitch, 2004; Vočadlo *et al*., 1999; Moroni *et al.*, 1999). Comparing these two phases should provide insights into the likely effects of the alloying of nickel with iron in the Earth's core. Specifically, it is necessary to determine whether NiSi is stable in the B2 (CsCl) structure at the conditions relevant to the deep Earth, as is known to be the case for FeSi (Vočadlo *et al*., 1999; Dobson *et al.*, 2002; 2003; Lord *et al*., 2010) and as is predicted to be the case for NiSi by recent *ab initio* calculations (Vočadlo *et al*. 2012). If these two end-members are isostructural it is reasonable to assume that they will form a solid solution. Consequently, the B2 structured FeSi phase postulated to be present within the Earth's core mantle boundary region (e.g.: Lord *et al*., 2010) could contain significant amounts of nickel leading to an (Fe,Ni)Si phase. Thus the question of the structure of NiSi at high pressure pertains directly to the phase relations of the deep Earth.

In a preceding paper on NiSi, Vočadlo *et al*. (2012) used static *ab initio* calculations to determine the stable structures and their equations of state at high pressure. These authors detail a sequence of predicted structural transitions. First, the MnP (B31) structure, which is the known stable phase at ambient conditions, transforms to the tetragonal γCuTi (B11) structure (space group: *P4/nmm*) at ~23 GPa and then to an orthorhombic structure (space group: *Pbma*) at ~61 GPa. As the pressure is raised further to ~168 GPa the orthorhombic FeB (B27) structure (space group: *Pnma*) becomes stable, followed by a final transition to the CsCl (B2) structure (space group: *Pm3m)* at ~247 GPa. Further to this, the authors have calculated equations of state for each of these phases, as well as for several others that are not stable at zero-Kelvin but may become stable at high temperatures. In particular, it was found that the difference in enthalpy between the ε-FeSi (B20) structure and the lowest enthalpy (most stable) structure is very small, dropping to as little as 8 meV atom^{-1} at ~60 GPa. However, as these calculations do not include temperature, they cannot tell us about the Clapeyron slopes of the phase boundaries between the predicted phases. Because these boundaries are likely to be sensitive to temperature we cannot use the calculations to say definitively which phases will be stable at the combined high-temperature and high-pressure conditions relevant to the deep Earth.

To address this issue, we have performed a set of synchrotron based X-ray powder diffraction experiments at high pressure in the diamond anvil cell on quenched laser-annealed samples up to 124 GPa. The primary aim of these experiments was to test whether the B2 (CsCl) structure is the stable form of NiSi at the conditions relevant to Earth's core, as predicted by the *ab initio* calculations of Vočadlo *et al*. (2012), and if so, to measure its room temperature equation of state. As will be described below, our successful pursuit of this aim has led to the detection of a minimum of two, and possibly all four of the non-ambient pressure structures predicted to be stable at zero-Kelvin by Vočadlo *et al*. (2012) that are listed in the preceding paragraph. Additionally, we have also detected one (and possibly two) of the structures which were considered by Vočadlo *et al*.

(2012) but found not to be stable at any pressure at zero-Kelvin, including the ε-FeSi (B20) structure previously mentioned, for which we have also obtained a room temperature equation of state. None of these high-pressure polymorphs of NiSi have been previously reported from experiment. Finally, we have measured the equation of state of the known B31 (MnP) structure, which is stable at ambient conditions.

Combining these observations with the results of the *ab initio* calculations has allowed us to make some preliminary inferences about the topology of the NiSi phase diagram. However, because of its apparent complexity and the fact that the experiments presented here were not optimized for the determination of phase relations (especially at the lower end of the relevant pressure and temperature range), further experimental work will be required to accurately map the phase diagram. This will require: 1) the acquisition of *in situ* structural information, to discriminate those phases which are thermodynamically stable from those that form during quench and 2) much longer annealing times to reduce phase co-existence. To access the full *P-T* space of interest, such a campaign may well require the use of laser-heated diamond anvil cells (for the very high-temperature region) and a combination of externally-heated diamond anvil cells and multi-anvil presses (for the moderate-temperature region). Such experiments are beyond the scope of the present study.

2. Methods

2.1 Starting material

The starting material for these experiments was prepared at the ISIS facility, Rutherford Appleton Laboratory, U.K. by arc-melting a stoichiometric mixture of nickel (99.99% purity) and silicon (99.999% purity) under ~ 500 mbar pressure of argon gas. The resulting boule was then broken up using a percussion mortar and several of the resulting pieces imaged using a scanning electron microscope and analysed using an electron microprobe. This revealed that the sample consisted of two phases. The first, majority, phase with the composition $Ni_{49.84(6)}Si_{50.16(6)}$ corresponding to near stoichiometric NiSi, forms >99% by volume of the sample. The second phase appears as thin veins (probably representing quench needles) and has a composition $Ni_{60.99(38)}Si_{39.01(38)}$ that corresponds closely to Ni_3Si_2 stoichiometry. An X-ray powder diffraction pattern of this material collected using a PANalytical X'pert PRO diffractometer with Co $K\alpha_1$ radiation also shows that NiSi is the dominant phase but that some very weak, broad, Bragg reflections were also present corresponding to those from δ-Ni_2Si (Toman, 1952). This strongly suggests that the minor phase seen in the scanning electron images is in fact an intergrowth of NiSi + δ-Ni_2Si which is too fine to be resolved by the microprobe, thus yielding an average composition of Ni_3Si_2. The composition of this phase, coupled with its texture, suggests it represents a quenched residual eutectic melt and that the bulk starting material is slightly nickel rich. This is not unexpected in silicides produced using the arc-melting process in which silicon is preferentially lost due to its greater volatility. Given the tiny volumetric contribution of this contaminant phase, it is unlikely to have significant effects on the results presented below.

2.2 Diamond anvil cell experiments

Two separate compression experiments were performed in this study, both using Princeton-type symmetric diamond anvil cells. The first (from 0 to 62 GPa) used anvils with a culet diameter of 250 μm, while the second (from 55 to 124 GPa) used beveled anvils with a 120 μm culet surrounded by an annulus with an 8° slope out to a diameter of 300 μm. In both cases rhenium was used as the gasket material, pre-indented to an initial thickness of ~40 μm and drilled out to form a central, cylindrical sample chamber approximately ⅓ the diameter of the culet. On compression, the gasket thickness and sample chamber diameter both decrease, to ~20 μm and ~¼ the diameter of the culet respectively, at the highest pressures reached.

For both compression experiments the sample consisted of a ~10 μm thick flake of NiSi taken from a foil produced by compressing the powdered sample (ground under ethanol in an agate mortar to a grain size on the order of 1 μm) between a pair of diamond anvils. This flake was sandwiched between two ~15 μm thick flakes of NaCl (99.99% purity) produced in the same fashion, which act as pressure medium, thermal insulator and pressure marker. Several grains of ruby (a few microns in size) were also added to the sample chamber so that pressure could be monitored by ruby fluorescence spectroscopy during off-line compression before the start of each X-ray diffraction measurement. To minimize moisture within the assembly, both the NiSi and NaCl were stored in an oven at 120°C and, after loading, each cell was heated at 120°C for 1 hour under an argon atmosphere before being sealed under the same conditions.

X-ray diffraction measurements were performed at beam-line 12.2.2 of the Advanced Light Source, Lawrence Berkeley National Laboratory, California, USA using a Gaussian monochromatic X-ray beam with $\lambda = 0.6199$Å with a nominal diameter (full width at half-maximum) of 10 μm (Caldwell *et al*., 2007). Before each X-ray diffraction pattern was acquired, the sample was annealed by laser heating to help reduce deviatoric stresses within the sample chamber in an effort to minimize broadening of the diffraction peaks. Laser heating was performed in a double-sided

geometry using two ytterbium fiber lasers with $\lambda = 1.09$ μm and a spot size of between 20 and 30 μm. Temperatures were measured at the surface of the sample on both sides using standard radiometric techniques (Walter & Koga, 2004). The annealing temperature was increased with increasing pressure, from 1400 K to 2700 K with the uncertainty in the measured temperature, estimated at ±150 K, incorporating both the reproducibility of calibration experiments (Yan *et al*., 2010) and variations in temperature during the annealing process. The sample was first ramped up to the target temperature by increasing the power to the lasers over a period of a few minutes, and once there, the laser was scanned around the entire sample for 10 minutes, to minimize the chance that any part of the sample might remain unreacted. After the annealing was complete, the samples were quenched rapidly to room temperature by cutting the power to the laser. Annealed samples were exposed to the X-ray beam for 60-180 seconds and the diffracted X-rays were collected on a Mar345 imaging plate. The sample to detector distance was calibrated using a LaB_6 standard. The 2D diffraction patterns were integrated into 1D spectra using the Fit2D program (Hammersley, 1997), which were in turn fitted and analysed using the Le Bail method (Le Bail *et al.*, 1988) as implemented in the GSAS suite of programs (Larson & Von Dreele, 2000; Toby, 2001). Sample pressure was determined using the equation of state of NaCl in the B1 structure below 30 GPa (Dorogokupets & Dewaele, 2007) and in the B2 structure above 30 GPa (Fei *et al.*, 2007). The reported uncertainties in pressure are the sum of the analytical uncertainty in the equations of state of NaCl and an additional uncertainty of 2% designed to take account of pressure gradients within the sample chamber. This is based on maximum measured pressure gradients of 2 GPa up to 150 GPa (i.e.: 1.3%) from a previous study in which a NaCl pressure medium, laser annealing and similar sample geometry were employed (Lord *et al.*, 2010).

It should be noted that the phase transitions reported below did not occur at room temperature. As described above, the samples were ramped rapidly to the target temperature, allowed to anneal, then rapidly quenched in the diamond anvil cell (i.e.: from high temperature to

room temperature within a second); this yields a temperature-time path along which the sample spends the majority of the total heating time at the target annealing temperature. Given that the reaction rate has an Arrhenius relationship with temperature (e.g.: Moore, 1963) the majority of the reaction is likely to have occurred at high temperature and as a result, the annealing temperature is likely to give a much more realistic idea of the conditions at which the phase transitions occurred. Therefore, the annealing temperature has been appended in parentheses to the reported pressures at which diffraction patterns were acquired. For estimates of the pressures of phase transitions, the appended temperature represents the mid-point between the annealing temperatures at which the diffraction patterns that bracket the transition were acquired, with the uncertainty calculated to encompass those temperatures.

3. Results

In the diffraction patterns collected in this study the diffracted intensity can be explained by NiSi, rhenium from the gasket and the NaCl pressure medium (in the B1 structure below 30 GPa and the B2 structure above 30 GPa); however very occasionally weak peaks are observed, most likely from other Ni_xSi_y phases (see §3.1). The presence of rhenium in all diffraction patterns is caused by a combination of the significant tails of the Gaussian X-ray beam (Caldwell *et al*., 2007), the very high X-ray scattering cross-section of rhenium and the reduction of the diameter of the sample chamber at high pressure. The greater intensity of the rhenium reflections in experiment two compared to experiment one is due to the necessarily smaller sample chamber required for this experiment (~30μm vs. ~60 μm at high pressure) in which much higher pressures were achieved (124 GPa vs. 62 GPa).

In the majority of diffraction patterns, more than one NiSi phase is present but in all cases one of the NiSi structures dominates the others. The dominant phase in order of increasing pressure is that with the MnP (B31), ε-FeSi (B20) and CsCl (B2) structure. Given the Arrhenius relationship between reaction rate and temperature (e.g.: Moore, 1963), these phases most likely represent those that were stable at the temperature at which the sample was annealed before it was quenched. These phases define a transition sequence at high temperature of B31 → B20 → B2 as pressure is increased. Six subordinate phases have also been detected with certainty and include the three described above. The fourth is orthorhombic and related to the FeB (B27) structure (hereafter called *Pnma*-II) and the fifth, also orthorhombic, has the space group *Pbma* (hereafter called *Pbma*-I). The peaks of the sixth subordinate phase are not inconsistent with yet another orthorhombic structure related to *Pnma*-II (hereafter called *Pnma*-III). Finally, several patterns contain peaks that may represent a seventh subordinate phase. This phase can be explained by several related structures, the tetragonal γ-CuTi (B11) structure (hereafter called *P4/nmm*), a distortion of this structure with space group *Pmmn* that has been detected in unpublished multi-anvil quench experiments (Ahmed,

2011, Pers. Comm.), or *Pbma*-I. However, it is not possible to discriminate between these three related structures with the present data. Barring *Pnma*-II, ε-FeSi (B20), and *Pmmn*, all of these phases were predicted to be stable for some pressures at zero-Kelvin in the *ab initio* calculations of Vočadlo *et al*. (2012). In some diffraction patterns, as many as three of these subordinate phases can be identified, in addition to the dominant phase. Assuming that no decomposition of the sample into phases with different stoichiometries occurs (i.e. that the phase diagram remains unary) the presence of four phases within a nominally single-component system clearly violates the phase rule, and indicates that one or more phases is metastable. Indeed, the presence of the subordinate phases can be explained by a combination of 1) metastable phase persistence, most likely due to certain regions of the sample (perhaps at the edges, or caught between the insulator and diamond anvil) having been heated for an insufficient time and/or to an insufficient temperature to overcome kinetic barriers, or 2) formation during quench as the cooling sample passes through the stability field of the phase in question. For the sake of clarity, given this dichotomy between the dominant and subordinate phases, we first discuss the transition sequence of the dominant phases, separated into two sections (§3.1 and §3.2), one for each of the two experiments performed, followed by a description of the associated *P-V* data and the fitting of equations of state (§3.3). We then treat the subordinate phases together in a separate section (§3.4).

3.1 Experiment one: 0-62 GPa

In the four diffraction patterns gathered at pressures up to 7 GPa (1400 K), NiSi was found to crystallize in the known B31 structure that is stable at ambient pressure (Fig. 1a). One weak peak at $2\theta = 8.6°$ ($d = 4.13$) which appears in a single pattern at 5 GPa may index to θ-Ni_2Si (note that a trace of δ-Ni_2Si was detected in the starting material, see §2.1). However, as this peak does not persist beyond this single pattern, has intensity below 3% relative to the strongest peak from the dominant B31-NiSi phase and no equation of state is available for θ-Ni_2Si, this assignment must be

considered tentative. It is however the most likely explanation, because this peak does not match the expected positions of any reflections from any of the NiSi polymorphs studied by Vočadlo *et al*. (2012), from the other known compounds in the Ni-Si system ($NiSi_2$, Ni_3Si or Ni_3Si_2) or from $Cr:Al_2O_3$ (ruby), which is the only other material expected to be present within the sample chamber.

In the next pattern, at 18 GPa (1700 K), new peaks appear, which index to the FeSi (B20) structure (Fig. 1b). Owing to the lack of diffraction data between 7 GPa (1400 K) and 18 GPa (1700 K), the location of this B31 → B20 transition cannot be determined beyond the precision defined by this bracket and it is thus estimated at 12.5±4.5 GPa and 1550±150 K. The presence of this phase transition is corroborated by the results of as yet unpublished multi-anvil press quench experiments, which were also analysed by X-ray diffraction (Ahmed, 2011, Pers. Comm.).

Until 43 GPa (1900 K) B20-NiSi remains the dominant phase (Fig. 2a) but in the next two patterns, taken at 49 GPa (1900 K) and 52 GPa (2000 K) three new weak peaks appear which can be indexed to the B2 structure (Fig. 2b). The *P-T* conditions of this B20 → B2 transition are estimated as 46±3 GPa and 1900±150 K. By 62 GPa (2100 K) - the highest pressure attained in the first experiment - these new peaks have grown in intensity to rival those of B20-NiSi.

3.2 Experiment two: 55-124 GPa

In the second experiment, weak reflections from B2-NiSi are present in the first two diffraction patterns, acquired at 54 GPa (1900±150 K) and 57 GPa (2000±150 K), increasing rapidly in intensity by 62 GPa (2100±150 K), in line with the results of the first experiment. In both experiments it was found that a small tetragonal distortion to the cubic B2 structure, of between 0.8% and -1.4%, was required to fit the peak positions accurately; a similar effect but with a smaller magnitude (up to -0.7%) was observed in the NaCl pressure medium that shares the same structure. This is the result of increasing deviatoric stresses caused by the hardening of the pressure medium

at high pressures. As was the case in experiment one, the B2-NiSi reverted entirely to B20-NiSi on decompression to ambient conditions.

3.3 Equations of state

We have not attempted to fit equations of state to those structures which only ever appear as subordinate phases (see §3), because either their diffraction peaks are too few and too weak to allow accurate volumes to be determined and/or they appear in too few diffraction patterns for an equation of state to be accurately fitted to the data. The *P-V* data for the dominant B31, B20 and B2 structures acquired from the compression experiments are presented in Fig. 3 and Table 1. The data were fitted using the third-order Birch-Murnaghan equation of state with the data all equally weighted, since the errors in volume and pressure were similar for all measurements. The resulting fitted parameters are presented in Table 2, together with the corresponding values from the *ab initio* calculations of Vočadlo *et al*. (2012).

For B31-NiSi, V_0 was fixed at the value determined by time-of-flight neutron powder diffraction for the same batch of starting material as was used in this study (Wood, Pers. Comm., 2011). This value is 1% lower than the *ab initio* result (Table 2; Vočadlo *et al*., 2012) which is in-keeping with the well known overestimation of volume, of around 1%, common in simulations that rely on the generalized gradient approximation. The limited number of *P-V* data for the B31-NiSi phase requires that K_0' also be fixed during fitting. We performed two fits: In the first, B31-1, $K_0' = 4$ (i.e.: the Birch-Murnaghan equation of state is truncated to second order) and in the second, B31-2, $K_0' = 4.47$ (the value determined from the zero-Kelvin *ab initio* simulations of Vočadlo *et al*., 2012). Both fits yield values of K_0 that are very similar to the *ab initio* values, with fit B31-2 having a marginally better residual of 3.33 versus 3.39 for fit B31-1 (throughout this paper, residual is taken to mean the sum of the squares of the differences between the observed pressure at each data point and that calculated from the equation of state). The scatter observed in the data for B31-NiSi is likely due to non-systematic errors that arise when trying to perform Le Bail refinements on phases with numerous closely spaced and overlapping peaks. This situation arises due to the

relatively low-symmetry of this orthorhombic phase and the short wavelength of the X-rays used for diffraction. Compounding the situation, the low pressures at which the B31-NiSi phase is stable require that laser annealing be performed at low temperatures (~1400 K) to ensure that the sample does not melt, leading to a less effective release of deviatoric stress and broader peaks due to the relative hardness of the NaCl pressure medium. To improve this situation, more precise equation of state measurements on this phase using a softer pressure medium such as He or Ne are planned for a future study.

In the case of the B20-NiSi phase, the data are much less scattered and cover a considerable degree of compression. Consequently, both K_0 and K_0' were left as free parameters in the fit while V_0 was fixed at the measured value upon release of pressure in the diamond anvil cell. As with the B31 structure, the measured V_0 is smaller than the value derived from the zero-Kelvin *ab initio* calculations of Vočadlo *et al*. (2012), in this case by 1.4% while K_0 is 11% smaller and K_0' is 20% larger. However, because these two parameters are so highly correlated, the experimental and *ab initio P-V* curves for B20-NiSi do not stray from one another by more than ±2.4% in volume up to 360 GPa. There is no evidence that the B1 → B2 transition in NaCl that occurs around 30 GPa, within the B20-NiSi stability field, has any effect on its compressibility, either due to the greater hardness of the B2 structure, the significant volume collapse across the transition, or any inconsistency between the equations of state of the two NaCl polymorphs used as the internal pressure standard.

Unlike the B31 and B20 structures, the B2-NiSi polymorph could not be recovered to ambient pressure and so no measured value for V_0 is available. Coupled with the relatively small range of compression over which *P-V* data for B2-NiSi have been collected, this leads to substantial uncertainties in the fitted equation of state parameters when all three are allowed to vary freely. It is clear, therefore, that either K_0' or V_0 must be fixed. To this end we have explored three options for

choosing reasonable values for one or other of these parameters. First of all, we fixed V_0 at 11.4±0.1 Å^3 atom^{-1}, a value obtained by subtracting 1.2% from the *ab initio* result (fit B2-1 in Table 2). This correction has been estimated by taking the average of the differences between the experimental and *ab initio* values of V_0 for the B31 and B20 structures (1.0% and 1.4% respectively; see Table 2); the uncertainty was chosen to be of a similar relative magnitude to this correction. This method yields a fit with a residual of 16.76 and a *P-V* curve which differs in volume from the *ab initio* curve by a maximum of 1.8% between 0 GPa and 360 GPa. The second option consists of fixing K_0' at 4.488 (fit B2-2 in Table 2), the value determined from the *ab initio* simulations of Vočadlo *et al*. (2012). This fit leads to a marginally better residual (15.23) than the previous attempt. While the resulting *P-V* curve underestimates the volume by 4.2% at ambient pressure compared with the *ab initio* curve, this mismatch diminishes with increasing pressure such that the two curves are identical above 330 GPa, which is unsurprising given that they share the same value of K_0'. The third and final option considered here involves fixing K_0' at 4 (i.e.: truncating the Birch-Murnaghan equation to 2nd order; fit B2-3 in Table 2). This fit yields the lowest residual (14.51) of all our attempts. The mismatch in the resulting *P-V* curve with the *ab initio* curve is 5.8% at ambient pressure but drops to 1.1% at 360 GPa.

Looking at Table 2, it is clear that none of the free parameters from the three fits described above match the corresponding *ab initio* values within their combined uncertainties. However, the differences are such that they lead to *P-V* curves which differ from the *ab initio* curve to only a small degree; for example, in fit B2-1, while K_0 is 14% smaller than the *ab initio* value, K_0' is 27% larger, leading to only marginal differences in volume at any given pressure. This trade-off between the pair of free parameters in each fit is apparent in their correlation coefficient, which is 99.35% for fit B2-1; this is the smallest correlation coefficient of any of the three fits described here. There is no clear reason why any of the three different fits described above should be considered the most

accurate. Therefore, our preferred fit is calculated by taking the centre point of the range of volumes defined by the three fits between 0 GPa and 360 GPa and fitting those points in turn to a 3rd order Birch-Murnaghan equation of state (fit B2-4 in Table 2). Compared to the *ab initio P-V* curve, our preferred fit underestimates the volume by 2.7% at ambient pressure, but the two curves are nearly identical above ~300 GPa. The uncertainty in the fitting parameters has been chosen so that the uncertainty in the resulting *P-V* curve encompasses the *P-V* curves of the three individual fits from which the preferred fit has been derived. This is the curve plotted in Fig. 3 and the one used in all subsequent discussions (see §4).

It should be noted that the small tetragonal distortion present in this phase above 60 GPa (see §3.2) might have a small systematic effect on the *P-V* data and the equation of state parameters derived from it. Future experiments using softer pressure media, such as He or Ne might, therefore, improve the accuracy of the equation of state, but the close correspondence with the *ab initio* results suggests that any systematic error caused by this effect is small.

3.4 The subordinate phases

After the B31 → B20 transition in experiment one (12.5±4.5 GPa and 1550±150 K), the B31 structure persists as a subordinate phase (with peak intensities <5% of the dominant B20-NiSi) until 49 GPa (1900 K), at which point it undergoes a distortion to the *Pnma*-II structure with which it shares the same space group (Fig. 2a,b). This spontaneous transition is predicted by the *ab initio* calculations of Vočadlo *et al*. (2012); the crystallographic relationship between the two phases is detailed in Fig. 2a and Fig. 6 of their paper. The *Pnma*-II structure remains present in all subsequent diffraction patterns, up to and including 62 GPa, the highest pressure reached in the first experiment. It is likely that the persistence of the B31 structure beyond the B31 → B20 transition is due to some part of the starting material remaining unheated throughout the experiment. Given that

the B31 → *Pnma*-II transition is achieved by a small shift in atomic positions without the re-arranging of bonds and that it occurs spontaneously on compression within the *ab initio* simulations, it is unlikely that there is a significant energy barrier associated with it that would require high-temperature annealing to overcome. Indeed, the high relative enthalpy of the *Pnma*-II phase (see Fig. 3 in Vočadlo *et al*., 2012) suggests that if this phase were to be heated significantly, it would almost certainly convert to the B20 structure, which supports the assumption that this phase, and the part of the B31 structure from which it formed, remained unheated throughout the experiment. The presence of rhenium in our diffraction patterns indicates that the entire sample chamber is being sampled by the X-ray beam. Thus the entire sample, including the edges, is contributing to the diffracted intensity. It is possible, therefore, that the unheated material described here resides at the sample edge, where proximity to the gasket prevented adequate laser annealing to transform it, due to the risk of reactions between the sample and gasket. Alternatively, a small piece of the starting sample may have become trapped, during loading, between the NaCl insulator and the diamond anvil, preventing it from being heated due to the large thermal conductivity of diamond.

After the B20 → B2 transition, the B20 structure remains present in every pattern, though the intensity of its peaks, already small after the transition, diminishes further at each subsequent compression and annealing step. The persistence of the B20 structure far beyond the pressure of the B20 → B2 transition is also observed in diamond anvil cell experiments on FeSi (Lord *et al.*, 2010) where it was interpreted to be the result of kinetic inhibition brought about by a high activation energy (Vočadlo *et al*., 1999). However, non-stoichiometry may provide a more compelling alternative explanation. If the B2 structure of NiSi is favored by excess metal, as is the case for both RuSi (Buschinger *et al.*, 1997) and FeSi (Dobson *et al.*, 2003), then as the transformation proceeds, the remaining B20 structured material will become increasingly silicon rich. Once the remaining

B20 structured material is richer in silicon than the solubility limit of silicon in the new B2 phase the reaction will cease, leaving a remnant of silicon rich B20 structured NiSi stable with respect to the further addition of silicon into the new B2 phase. This sequence requires that the NiSi B20 structure display some propensity for solid solution, as it is known to do in both the RuSi and FeSi systems. Note that the explanation used for the persistence of the B31 structure beyond the B31 → B20 transition cannot be used to explain the persistence of the B20 structure beyond the B20 → B2 transition; if unheated material was present, it would probably have remained in the B31 structure or undergone a series of distortions, first to the *Pnma*-II structure (described above) and then to the *Pnma*-III structure (Vočadlo *et al*., 2012).

Between 7 GPa (1400 K; Fig. 1b) and 49 GPa (1900 K; Fig. 2b) an additional subordinate phase is also present in some, but not all patterns. The peak positions are not inconsistent with the *Pbma*-I structure but they can also be explained by the related *P4/nmm* or *Pmmn* phases (see §3); it is not possible to distinguish between these structures with certainty, given the current data. The *P4/nmm* structure was predicted to be stable between 23 GPa and 61 GPa at zero-Kelvin (Vočadlo *et al*., 2012), although there is likely to be a considerable uncertainty in these transition pressures, perhaps as much as ±10 GPa. An orthorhombically distorted variant of the *P*4/*nmm* structure, with space group *Pmmn* has been detected very recently in as yet unpublished quenched multi-anvil experiments (J. Ahmed, Pers. Comm., 2011); this distortion was not considered in the *ab initio* calculations of Vočadlo *et al*. (2012). The diffraction peaks from this phase, whatever its structure may be, result from the integration of a few spots on the 2-D Debye-Scherrer ring suggesting that only a few crystals are contributing to the diffracted signal, unlike the dominant phase in each pattern, which is usually associated with continuous powder rings. This texture, combined with the close co-incidence between the pressure range of this phase and the pressure range in which two candidate structures are found (*P4/nmm* in the *ab initio* calculations and *Pmmn* in the multi-anvil

quench experiments) suggests that this phase enjoys a field of stability at temperatures below those at which our samples were equilibrated and therefore formed as the sample quenched through it. Additional experiments will clearly be needed to determine the stability fields of these various candidate structures and to make a definitive assignment.

A similar argument can be made for the presence of the *Pbma*-I structure (Vočadlo *et al*., 2012), which we find, in this case unambiguously, between 54 GPa (1900 K) and 124 GPa (2700 K), the highest pressure reached in this study. Again, this range fits well with the zero-Kelvin stability predictions for this structure from the *ab initio* simulations (61 GPa to 168 GPa). Again, the Debye-Scherrer rings associated with this phase are spotty rather than continuous.

Between 102 GPa (2500 K) and 124 GPa (2700 K) two peaks are present which are not inconsistent with the cell parameters of the *Pnma*-III phase as predicted by the *ab initio* simulations, although this assignment is not certain. The simulations indicate that this phase should not be stable until beyond 168 GPa. Nevertheless, the fact that the *Pbma*-I phase and probably also the *P4/nmm* phase, or its orthorhombically distorted *Pmmn* variant, appear in our experiments in the same order as they were predicted to occur at zero-Kelvin in the *ab initio* simulations is strong, if not conclusive evidence that these phases formed on quench. If this is the case, these subordinate phases contain information about the topology of the NiSi phase diagram. However, given that we cannot exclude alternative explanations for the existence of these phases, including the very slight non-stoichiometry of our starting material, we refrain from constructing the phase diagram at this stage and prefer to wait for the results of future experiments which are optimized for the detailed mapping of phase relations. It is intriguing to note, however, that it is possible to formulate a self-consistent phase diagram with a feasible topology which broadly agrees with the zero-Kelvin simulations by making just two assumptions both of which we believe to be reasonable: 1) that the *Pnma*-II structure is metastable, and forms from unreacted (and thus probably unheated) B31

structured starting material and 2) that the *Pbma*-I and *Pnma*-III structures (as well as the *P4/nmm*, or *Pmmn*, phase, if confirmed) formed as the sample cooled through their respective stability fields.

4. Discussion

4.1 NiSi in the CsCl (B2) structure

The experiments reported here bracket the B20 → B2 transition at 46±3 GPa and 1900±150 K while the *ab initio* simulations indicate that the B2 structure becomes stable above 247 GPa at zero-Kelvin. By combining these two *P-T* points we can calculate that the phase boundary between the B2 structure and the lower pressure structures adjacent to it has a Clapeyron slope of ~-9.5 K GPa^{-1}. Note that although we cannot be certain of the topology of the NiSi phase diagram between these two points, the fact that the B20 structure is not stable at zero-Kelvin requires that at least one additional phase boundary must intersect the low-pressure boundary of the B2 stability field, which must create an inflexion. Schreinemaker's rules require that this inflexion cause the B2 stability field to be widened even further. We can be nearly certain then, excepting the possibility of further phase transitions at conditions beyond the range of the present experimental study to structures not considered in the simulations (Vočadlo *et al.*, 2012), that B2-NiSi is the stable structure throughout most of the Earth's mantle and the entirety of its core. Therefore, at the conditions of the lowermost mantle, where FeSi is potentially present (Lord *et al*., 2010; Dubrovinsky *et al*., 2003), NiSi and FeSi will be isostructural and are likely to form a solid solution. Given that the postulated formation mechanisms for FeSi in the lowermost mantle rely on the nickel-bearing core alloy as their source, we would in fact expect a single (Fe,Ni)Si phase to form. In the inner core, however, where plausible alloys in the Fe-Ni-Si ternary will plot near the iron-rich apex, recent phase relations studies suggest that a single phase with the hexagonally close packed structure will form instead (Asanuma *et al*., 2008; 2011; Sakai *et al*., 2011). Although additional *in situ* X-ray diffraction experiments will be required to elucidate the detailed topology of the NiSi phase diagram, these broad conclusions seem robust.

Such a transition was not entirely unexpected; a similar B20 → B2 transition is observed in FeSi (Dobson *et al*., 2002; Vočadlo *et al.*, 1999) while RuSi is known to be stable in both structures at ambient pressure (e.g.: Göransson *et al.*, 1995). There are additional parallels in the B20 → B2 transition between NiSi and FeSi: 1) FeSi also has a negative Clapeyron slope (although it is steeper and offset to lower pressures), and 2) the volume decrease at the transition is similar (0.8% for NiSi compared to 1.1% for FeSi), as determined from the equations of state for B20-FeSi (Ross, 1996) and B2-FeSi (Sata *et al*., 2010). This similarity in volume decrease at the transition should, however, be considered with caution, because it is based on a room temperature transition pressure (105 GPa) for FeSi extrapolated from a measurement of the slope of the phase boundary at high temperature (Lord *et al.*, 2010).

The experimental and *ab initio P-V* curves for B2-NiSi, calculated using the equation of state parameters in Table 2 are nearly identical above 300 GPa (Fig. 4) with a maximum difference (which occurs at ambient pressure) of 2.7% in volume. For B2-FeSi, at ambient pressure, the *ab initio* simulations (Vočadlo *et al*., 1999) yield a volume that is smaller than the experimentally determined value (Sata *et al*., 2010), which is the opposite behaviour to that usually seen in *ab initio* calculations employing the generalized gradient approximation but is common in iron-bearing systems. This is followed by a volume crossover (~30 GPa) and then a significant divergence between the *ab initio* and experimental results at higher pressures (Fig. 4). Essentially identical differences are observed if the *ab initio* equation of state for B2-FeSi of Caracas and Wentzcovitch (2004) is used, although in this case the volume at high pressure (6.654 $Å^3$ $atom^{-1}$ at 330 GPa) agrees a little better with that expected from experiment (see Fig. 4). This means that conclusions drawn from the comparison of the physical properties (specifically density) of NiSi and FeSi in the B2 structure are strongly dependant upon whether we use the *ab initio* or experimental equations of

state. Given that the B2 structure is the one relevant to the Earth's core, the following values are all calculated at 330 GPa, the pressure at the boundary between the inner and outer core.

The *ab initio* equations of state (Vočadlo *et al*., 1999; Vočadlo *et al*., 2012) indicate that at 330 GPa B2-NiSi is denser than B2-FeSi by 5.9±0.6%; not only is the nickel atom heavier, but the volume of B2-NiSi is smaller than B2-FeSi, due to a volume crossover at ~170 GPa. If the equation of state for B2-FeSi of Caracas and Wentzcovitch (2004) is used, this density difference reduces to 3.3±0.7%. No comparison can be made with the *ab initio* equation of state for B2-FeSi of Moroni et al. (1999) because the authors do not report their value of K_0'. In contrast, according to the experimental equations of state, the density of B2-NiSi (10.82±0.25 g cm^{-3}) is 1.1±2.5% *lower* than B2-FeSi (10.94±0.10 g cm^{-3}), though the difference is clearly within the mutual uncertainties. Both of the published experimental equations of state for B2-FeSi agree very closely (Sata *et al.,* 2010; Dobson *et al*., 2003) such that this result is almost completely insensitive to which of these is used. It follows then that for the B2 structures, the discrepancy in the quantity $\rho_{NiSi} - \rho_{FeSi}$ between the experimental and *ab initio* techniques at 330 GPa lies somewhere between 4.4±3.2% and 7.0±3.1%. Given the large uncertainty on this density difference it is clear that further work is needed to determine the densities more precisely.

4.2 NiSi in the ε-FeSi (B20) structure

The B31 → B20 transition occurs at 12.5±4.5 GPa and 1550±150 K. Although the B20 structure is not stable at any pressure at zero-Kelvin in the simulations, the lines representing the B31 and B20 structures cross at 33.5 GPa on the ΔH vs. P plot (Fig. 3 in Vočadlo *et al*. 2012), representing a metastable transition point. Given these two P-T points, we can estimate the Clapeyron slope of the transition as -74 K GPa^{-1}. This leads to a transition pressure of 17 GPa at 300 K, with an associated volume decrease of 6%. As mentioned in the introduction, the difference

in enthalpy between B20-NiSi and the structures which are predicted to be stable is only ~30 meV at 18 GPa, and decreases to as little as 8 meV at 60 GPa. Such a small enthalpy difference could easily be overcome at the high temperatures reached during the laser annealing of the sample and so the appearance of this phase is not surprising.

As was the case with B2-NiSi, a comparison of the experimental and *ab initio P-V* curves for B20-NiSi, calculated using the equation of state parameters in Table 2 shows excellent agreement (Fig. 5). Although the *ab initio P-V* curve yields higher volumes at all pressures up to at least 150 GPa, the offset is never more than 1.8%. The closeness of this match is all the more impressive when we consider that simulations that employ the generalized gradient approximation are known to overestimate volume by ~1%. In contrast, B20-FeSi behaves in a remarkably similar way to B2-FeSi showing a systematic difference between the *ab initio* and experimental equations of state (see §4.1). As was the case for B2-FeSi, the *ab initio* simulations of Vočadlo *et al*. (1999) exhibit the unusual behaviour of yielding a volume that is smaller than the experimentally determined value (Wood *et al.*, 1995). This is followed by a volume crossover, in this case at ~15 GPa, after which the experimental and *ab initio P-V* curves diverge significantly (Fig. 5). We can employ the same approach used for the B2 structures (see §4.1) to compare how the two techniques (simulation vs. experiment) effect estimates of the relative densities of B20-NiSi and B20-FeSi.

At 150 GPa, the *ab initio* equations of state (Vočadlo *et al*., 1999; Vočadlo *et al*., 2012) indicate that B20-NiSi is the denser phase, by 1.5±0.5%; the greater mass of the nickel atom more than compensates for the greater volume of B20-NiSi. If the equation of state for B20-FeSi of Caracas and Wentzcovitch (2004) is used, this density difference increases to 3.4±0.2% (for B20-FeSi the *ab initio* equations of state of Vočadlo *et al*. (1999) and Caracas and Wentzcovitch (2004) run almost exactly parallel to each other with the latter having a volume that is greater by 0.016 $Å^3$ $atom^{-1}$). As with B2-FeSi, no comparison can be made with the *ab initio* equation of state for B2-NiSi of Moroni et al. (1999) because the authors do not report their value of K_0'. In contrast, the

density of B20-NiSi is 1.8±1.0% *lower* than B20-FeSi according to the experimental equations of state at the same pressure conditions. The majority of published equations of state for B20-FeSi are so similar (Guyot & Zhang, 1995; Wood *et al.*, 1995; Ross, 1996; Guyot *et al.*, 1997) that this analysis is largely insensitive to which is used. Thus, the difference in the quantity ρ_{NiSi} - ρ_{FeSi} between the experimental and *ab initio* techniques at 150 GPa is between 3.3±1.1% and 5.2±1.1%. This difference is clearly statistically significant, unlike the difference for the B2 structures discussed in §4.1, primarily because of the smaller uncertainty in the experimental equation of state for B20-NiSi compared with B2-NiSi.

4.3 Comparisons with other stoichiometries

Comparing Fig. 4 and Fig. 5, it is clear that the *P-V* systematics of both the B2 and B20 structures are strikingly similar. Further, the difference between ρ_{NiSi} - ρ_{FeSi} between the *ab initio* and experimental methods is of the same sign in both structures. The question is from where does this discrepancy arise? Two points are pertinent here: 1) there is close agreement between the *ab initio* and experimental *P-V* curves both for B2-NiSi and B20-NiSi and 2) the *P-V* curves derived from the majority of published experimental equations of state for B20-FeSi agree very closely with each other as do both published experimental equations of state for B2-FeSi. This hints that the problem may lie with the *ab initio* simulations performed on FeSi (Vočadlo *et al*., 1999; Caracas and Wentzcovitch, 2004). The fact that these discrepancies occur in both the B2 and B20 structures suggests that the problem is not related to the structure itself, but perhaps instead with the theoretical description of the iron atom. One possible manifestation of this potential problem are the differences between the experimentally determined values of V_0 and those determined by the *ab initio* simulations that rely on the generalised gradient approximation. Such calculations would be expected to significantly overestimate V_0 compared to experiment (as indeed they do for B20-NiSi, B2-NiSi and B31-NiSi, by between 1.0% and 3.7%). However, for B20-FeSi the *ab initio*

simulations (Vočadlo *et al*. 1999; Caracas and Wentzcovitch, 2004) underestimate V_0 compared to experiment, by between 0.2% and 1.6%. For B2-FeSi the *ab initio* simulations of Vočadlo *et al*., 1999 also underestimate V_0 compared to experiment, in this case by 0.7%. The only exception to this behaviour are the *ab initio* simulations for B2-FeSi of Caracas and Wentzcovitch (2004) which barely overestimate V_0 compared to experiment, but by less than 0.02%. Possible reasons for the discrepancy between the experimental equation of state for B20-FeSi and that from *ab initio* simulations were discussed by Vočadlo *et al*. (2000), who concluded that it was unlikely to have arisen from either slight variations in the stoichiometry of the material used in the experiments or from any failure to incorporate magnetism correctly in the simulations. In view of this, it is instructive to look at whether similar behaviour is evident in iron silicides with different stoichiometries. Errandonea *et al.* (2008) saw a similar underestimate in the volume of both α-Fe_2Si and Fe_5Si_3 (xifengite) in their *ab initio* calculations at ambient pressure as compared with their experimentally determined values, while calculations by the same authors on δ-Ni_2Si yielded the expected overestimate. All of these simulations employed the generalized gradient approximation. However, it is not always the case that *ab initio* simulations on iron silicides overestimate volume: Moroni *et al*. (1999) found that the opposite is true for Fe_3Si (suessite) and both α- and β-$FeSi_2$. Given this limited dataset however, it is not currently possible to draw any firm conclusions about the reasons for the discrepancy observed in the monosilicides.

Acknowledgements

O. T. L. acknowledges support from the Natural Environment Research Council at UCL (NERC Grant NE/H003975/1). The experimental work at the Advanced Lights Source, Lawrence Berkeley National Laboratory was additionally supported by NERC grant NE/H003541/1 awarded to Prof. M. J. Walter at the University of Bristol. O. T. L. would also like to thank Alastair McDowell, Jason Knight and Jinyuan Yan for their technical assistance at beam-line 12.2.2 of the ALS. We also wish to thank Dr Devashibhai Adroja and Dr Kevin Knight (ISIS Facility, Rutherford Appleton Laboratory, U.K.) for assistance with the sample preparation and Jabraan Ahmed (Dept. Earth Sciences, UCL) for helpful discussions. Finally, the authors would like to acknowledge three anonymous reviewers whose comments helped to significantly improve the manuscript.

References

Ahmed, J. (2011). Personal communication.

Acker, J., van den Berg, G. J. K., Bohmhammel, K., Kloc, Ch. & van Miltenberg, J. C. (1999). *Thermo. Acta*., **339**, 29-33.

Allègre, C. J., Poirier, J.-P., Humler, E. & Hofmann, A. W. (1995). *Earth Planet. Sci. Lett.*, **134**, 515-526.

Asanuma, H., Ohtani, E., Sakai, T., Terasaki, H., Kamada, S., Hirao, N., Ohishi, Y. (2011). *Earth Planet. Sci. Lett.*, **310**, 113-118.

Asanuma, H., Ohtani, E., Sakai, T., Terasaki, H., Kamada, S., Hirao, N., Sata, N., Ohishi, Y. (2008). *Geophys. Res. Lett.*, **35**, L12307.

Badro, J., Fiquet, G., Guyot, F., Gregoryanz, E., Occelli, F., Antonangeli, D., d'Astuto, M. (2007). *Earth Planet. Sci. Lett.*, **254**, 233-238.

Buschinger, B., Geibel, C., Diehl, J., Weiden, M., Guth, W., Wildbrett, A., Horn, S. & Steglich, F. (1997). *J. Alloys Comput.*, **256**, 57-60.

Caldwell, W. A., Kunz, M., Celestre, R. S., Domning, E. E., Walter, M. J., Walker, D., Glossinger, J., MacDowell, A. A., Padmore, H. A., Jeanloz, R. & Clark, S. M. (2007). *Nuclear Inst. Meth. Phys. Res. A*, **582**, 221-225.

Caracas, R. & Wentzcovitch, R. (2004). *Geophys. Res. Lett*., **31**, L20603.

Connétable, D. & Thomas, O. (2009). *Phys. Rev. B*, **79**, 094101.

Detavernier, C., Lavoie, C. & d'Heurle, F. M. (2003). *J. App. Phys.*, **93**(5), 2510-2515.

Dobson, D. P., Vočadlo, L., Wood, I. G. (2002). *Am. Min.*, **87**, 784-787.

Dobson, D. P., Chrichton, W. A., Bouvier, P., Vočadlo, L., Wood, I. G. (2003). *Geophys. Res. Lett.*, **30**(1), 1014.

Dorogokupets, P. I. & Dewaele, A. (2007). *High Pressure Res.*, **27**(4), 431-446.

Errandonea, D., Santamaría-Perez, D., Vegas, A., Nuss, J., Jansen, M., Rodríguez-Hernandez, P., Muñoz, A. (2008). *Phys. Rev. B*, **77**, 094113.

Fei, Y., Ricolleau, A., Frank, M., Mibe, K., Shen, G. & Prakapenka, V. (2007). *Proc. Natl. Acad. Sci. U.S.A*, **104**, 9182-9186.

Göransson, K., Engström, I. & Noläng, B. (1995). *J. Alloys Comput.*, **219**, 107-110.

Guyot, F., Zhang, J., Martinez, I., Matas, J., Ricard, Y. & Javoy, M. (1997). *Eur. J. Min.*, **9**, 277-285.

Guyot, F. & Zhang, J. (1995). *Terra Nova*, (Abs. Supp. 1) **7**, 84.

Hammersley, A. P. (1997). FIT2D: an introduction and overview, Technical Report ESRF-97-HA-02T, ESRF, Grenoble.

Helffrich, G. (2011). *Geophys. J. Int.*, doi: 10.1111/j.1365-246X.2011.05295.x

Helffrich, G. & Kaneshima, S. (2010). *Nature*, **468**, 807-810.

Helffrich, G. & Kaneshima, S. (2004). *Science*, **306**, 2239-2242.

Kuwayama, Y., Sawai, T., Hirose, K., Sata, N., Ohishi, Y. (2009). *Phys. Chem. Minerals*, **36**, 511-518.

Kuwayama, Y., Hirose, K., Sata, N., Ohishi, Y. (2008). *Earth Planet. Sci. Lett.*, **273**, 379-385.

Larson, A. C. & Von Dreele, R. B. (1994). General Structure Analysis System (GSAS), Los Alamos National Laboratory Report LAUR 86-748.

Le Bail, A., Duroy, H. & Fourquet, J. L. (1988). *Mater. Res. Bull.* **23**, 447-452.

Lin, J.-F., Campbell, A. J., Heinz, D. L. (2003a). *J. Geophys. Res.*, **108**, 2045.

Lin, J.-F., Struzhkin, V. V., Sturhahn, W., Huang, E., Zhao, J., Hu, M. Y., Alp, E. E., Mao, H.-K., Boctor, N. & Hemley, R. J. (2003b). *Geophys. Res. Lett.*, **30**(21), 2112.

Lin, J.-F., Heinz, D. L., Campbell, A. J., Devine, J. M., Mao, W. L., Shen, G. (2002). *Geophys. Res. Lett.*, **29**, 1471.

Lord, O. T., Walter, M. J., Dobson, D. P., Armstrong, L., Clark, S. M., Kleppe, A. (2010). *J. Geophys. Res.*, **115**, B06208.

Mao, W. L., Campbell, A. J., Heinz, D. L., Shen, G. (2006). *Phys. Earth Planet. Sci.*, **155**, 146-151.

Moore, W. J., (1963). *Physical Chemistry*. London: Longmans.

Morard, G., Andrault, D., Guignot, N., Siebert, J., Garbarino, G., Antonangeli, D. (2011). *Phys. Chem. Minerals*, **38**, 767-776.

Moroni, E. G., Wolf, W., Hafner, J. & Podloucky, R. (1999). *Phys. Rev. B*, **59**(20), 12860-12871.

Rabadanov, M. Kh. & Ataev, M. B. (2002a). *Cryst. Rep.*, **47**(1), 40-45.

Rabadanov, M. Kh. & Ataev, M. B. (2002b). *Cryst. Rep.*, **47**(3), 379-382.

Ross, N. L. (1996). *Acta Cryst. A*, **52**, C-530.

Sakai, T., Ohtani, E., Hirao, N., Ohishi, Y. (2011). *Geophys. Res. Lett.*, **38**, L09302

Sata, N., Hirose, K., Shen, G., Nakajima, Y., Ohishi, Y. & Hirao, N. (2010). *J. Geophys. Res.*, **115**, B09204.

Toby, B. H. (2001). *J. App. Cryst.*, **34**, 210-213.

Toman, K. (1951). *Acta Cryst.*, **4**, 462-464.

Toman, K. (1952). *Acta Cryst.*, **5**, 329-331.

Vočadlo, L., Wood, I. G. & Dobson, D. P. (2012). *J. App. Cryst.* **45**, 186-196.

Vočadlo, L., Price, G. D. & Wood, I. G. (1999). *Acta Cryst. B*, **55**, 484-493.

Vočadlo, L., Price, G. D. & Wood, I. G. (2000). *Acta Cryst. B*, **56**, 369-376.

Walter, M.J. & Koga, K. T. (2004). *Phys. Earth Planet. Inter.*, **143-144**, 541-558.

Wilson, D. F., Cavin, O. B. (1992). *Scripta Metall. Material.*, **26**, 85-88.

Wood, I. G. (2011). Personal communication.

Wood, I. G., Chaplin, T. D., David, W. I. F., Hull, S., Price, G. D. & Street, J. N. (1995). *J. Phys. Condens. Matter*, **7**, L475- L479.

Yan, J., Knight, J., Kunz, M., Raju, S. V., Chen, B., Gleason, A. E., Godwal, B. K., Geballe, Z., Jeanloz, R. & Clark, S. M. (2010). *J Phys. Chem. Solids*, **71**, 1179-1182.

Figure Captions

Figure 1. Diffraction data (black crosses) bracketing the B31-B20 transition, modeled using the Le Bail method (red line). The background (green line) and residual (blue line) are also shown. (a) At 7 GPa (1400 K) NiSi is in the B31 structure. The single unindexed peak at $2\theta = 10.9°$ (d = 3.26 Å) possibly represents a trace of the orthorhombic *Pbma*-I phase (see §3.4 for details). Tick marks indicate the positions of the peaks from (top down): B31-NiSi, B1-NaCl and Re (b) At 18 GPa (1700 K) NiSi is in the B20 structure. Unreacted B31-NiSi is still present, as is a trace of an orthorhombic or tetragonal phase, either *Pbma*-I, *Pmmn* or *P4/nmm*, (see §3.4 for details). Tick marks indicate the positions of the peaks from (top down): B20-NiSi, B31-NiSi, B2-NaCl, Re and *P4/nmm* NiSi.

Figure 2. Diffraction data (black crosses) bracketing the B20-B2 transition, modeled using the Le Bail method (red line). The background (green line) and residual (blue line) are also shown. (a) At 43 GPa (1900 K) NiSi is in the B20 structure. A trace of unreacted B31-NiSi is also present. Tick marks indicate the positions of the peaks from (top down): B20-NiSi, B31-NiSi, B1-NaCl and Re. (b) At 49 GPa (1900 K) peaks from the B2 structured NiSi polymorph appear but are still weak compared to the dominant peaks from B20-NiSi. Traces of both *Pnma*-II and an additional orthorhombic or tetragonal phase (either *Pbma*-I, *Pmmn* or *P4/nmm*) are also present (see §3.4 for details). Tick marks indicate the positions of the peaks from (top down): B2-NiSi, B20-NiSi, B2-NaCl, Re, *Pnma*-II NiSi and *P4/nmm* NiSi.

Figure 3. *P-V* plot for (in order of decreasing volume) B31-NiSi (red), B20-NiSi (blue) and B2-NiSi (green). The curves represent equally weighted fits to the data using the Birch-Murnaghan equation of state truncated to the 3rd order. Dashed lines are extrapolations beyond the region of

data coverage. Circles represent data from experiment one; squares represent data from experiment two (see text). The corresponding *P-V* data are presented in Table 1 and the equation of state parameters in Table 2. Volume error bars are smaller than the symbol size.

Figure 4. *P-V* curves for NiSi (thin blue lines) and FeSi (thick red lines) in the B2 structure. The solid lines represent experimentally determined equations of state from this study for NiSi and from Sata *et al.* (2010) for FeSi. The dashed lines represent equations of state determined from *ab initio* simulations from Vočadlo *et al*. (2012) for NiSi and Vočadlo *et al*. (1999) for FeSi; the red circle indicates the predicted volume of B2-FeSi at 330 GPa from the equation of state of Caracas and Wentzcovitch (2004).

Figure 5. *P-V* curves for NiSi (thin blue lines) and FeSi (thick red lines) in the B20 structure. The solid lines represent experimentally determined equations of state from this study for NiSi and from Ross (1996) for FeSi (taking the value of V_0 from Wood *et al.*, 1995). The dashed lines represent equations of state determined from *ab initio* simulations from Vočadlo *et al*. (2012) for NiSi and Vočadlo *et al*. (1999) for FeSi; the red circle indicates the predicted volume of B20-FeSi at 150 GPa from the equation of state of Caracas and Wentzcovitch (2004).

Table 1: Unit-cell parameters of the B31 (MnP), B20 (ε-FeSi) and B2 (CsCl) structured phases of NiSi as a function of pressure.

P (GPa)	*a* (Å)	*b* (Å)	*c* (Å)	*V* (Å^3 atom^{-1})
B31 (MnP) structured NiSi[a]				
0.02(2)	5.182(1)	3.3558(6)	5.611(1)	12.196(3)
2.5(1)	5.244(1)	3.211(1)	5.669(1)	11.931(2)
5.0(2)	5.329(1)	3.1410(3)	5.6663(5)	11.864(2)
6.9(3)	5.282(1)	3.1039(5)	5.674(3)	11.628(4)
17.0(4)	5.046(1)	3.316(2)	5.324(3)	11.134(8)
22.6(5)	5.107(4)	3.234(2)	5.294(2)	10.930(7)
28(1)	4.85(1)	3.469(1)	5.063(3)	10.65(2)
B20 (ε-FeSi) structured NiSi				
0.0001	4.5050(5)	-	-	11.4289(1)
17.0(4)	4.38115(5)	-	-	10.5118(4)
22.6(5)	4.3541(4)	-	-	10.318(3)
28(1)	4.3246(2)	-	-	10.110(1)
36(1)	4.2862(1)	-	-	9.843(1)
42(1)	4.2652(1)	-	-	9.699(1)
49(1)	4.2366(1)	-	-	9.505(1)
52(1)	4.2269(4)	-	-	9.440(3)
54(1)	4.2213(2)	-	-	9.403(1)
57(2)	4.2140(2)	-	-	9.354(3)
61(1)	4.1959(2)	-	-	9.234(2)
62(1)	4.1918(1)	-	-	9.207(1)
68(1)	4.1794(4)	-	-	9.125(4)
73(2)	4.1678(4)	-	-	9.049(3)
77(2)	4.1552(5)	-	-	8.968(3)
85(2)	4.134(1)	-	-	8.832(6)
B2 (CsCl) structured NiSi[b]				
61(1)	2.6394(3)	-	2.612(1)	9.098(4)
62(1)	2.6361(4)	-	2.6151(4)	9.086(2)
68(1)	2.6288 (3)	-	2.6033(3)	8.995(1)
73(2)	2.6201(2)	-	2.5834(3)	8.868(1)

77(2)	2.6101(2)	-	2.5879(3)	8.815(1)
85(2)	2.5805(2)	-	2.5986(2)	8.652(1)
101(2)	2.5788(2)	-	2.5503(3)	8.481(1)
104(2)	2.5751(2)	-	2.5388(3)	8.418(1)
116(3)	2.5543(3)	-	2.5273(5)	8.245(2)
124(3)	2.5275(3)	-	2.5473(6)	8.137(1)

Values in parentheses represent the uncertainty in the final digit.
[a]It is interesting to note that the *b*-axis of the B31 (MnP) phase appears to show negative linear compressibility at high pressure, as predicted by the computer simulations of Vočadlo *et al*. (2012); more precise measurements are, however, required to confirm this.
[b]The B2 phase includes a small tetragonal distortion.

723

Table 2: Third-order Birch-Murnaghan Equation of state parameters of the B31 (MnP), B20 (ε-FeSi) and B2 (CsCl) structured phases of NiSi (for details see text).

	This Study			Vočadlo *et al*. (2012)		
Structure	V_0 (Å^3 atom^{-1})	K_0 (GPa)	K_0'	V_0 (Å^3 atom^{-1})	K_0 (GPa)	K_0'
B31-1	12.1499(1)[b]	165(3)	4[a]	12.277(3)	160.572(2)	4.47(6)
B31-2	12.1499(1)[b]	161(3)	4.47[a]			
B20	11.4289[a]	161(3)	5.6(2)	11.593(3)	180.143(4)	4.48(1)
B2-1	11.4(1)[c]	148(7)	5.5(3)			
B2-2	11.0(1)	210(10)	4.488[a]	11.5020(5)	173.1770(6)	4.488(2)
B2-3	10.87(7)	240(10)	4[a]			
B2-4	11.09(5)	200(9)	4.6(1)			

[a]Values fixed during fitting.
[b]From unpublished neutron diffraction data on the same batch of starting material (Wood, 2011)
[c]Value derived by subtracting 1.1% from the value reported in Vočadlo *et al*. (2012); see text. The uncertainty encompasses the magnitude of the correction.

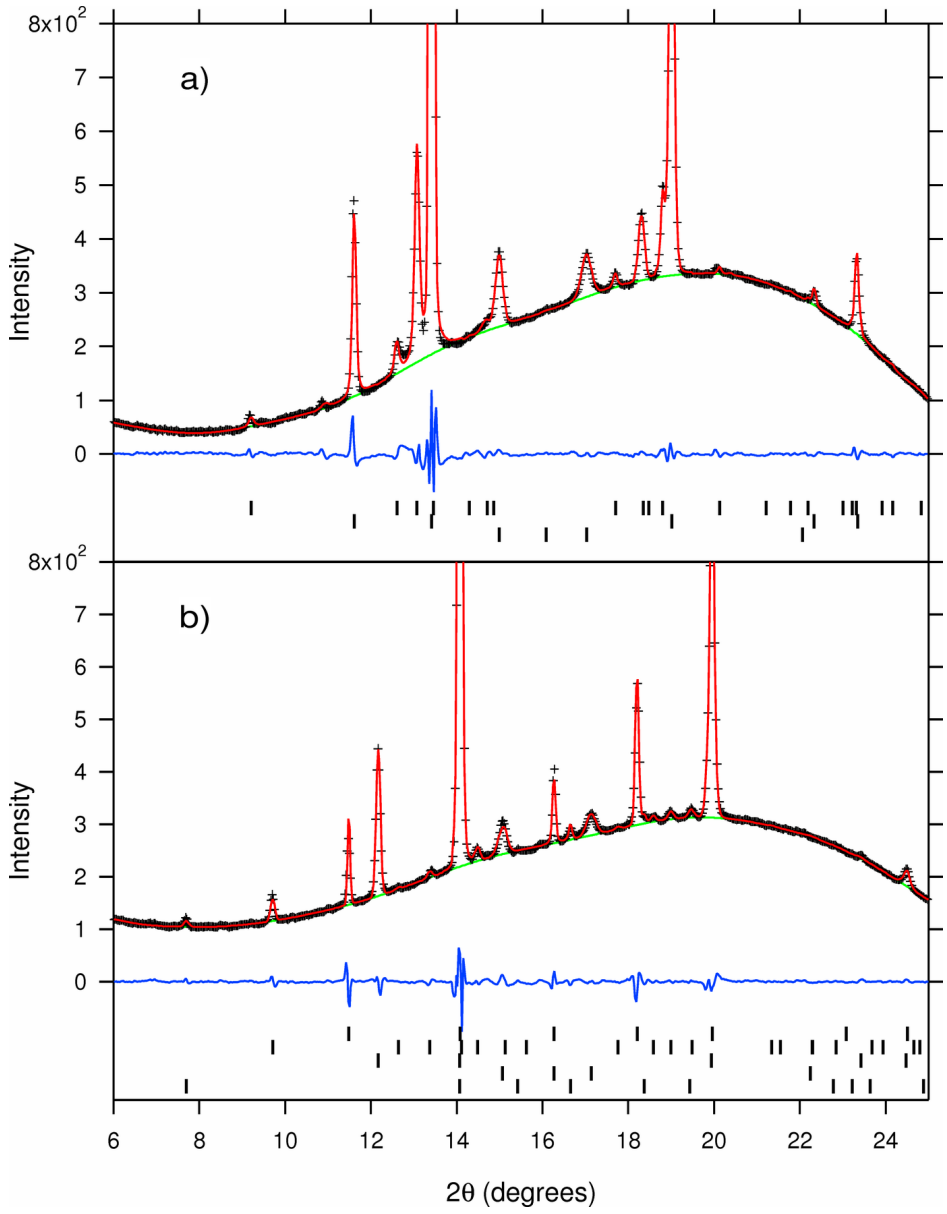
8x10^2
a)
Intensity
8x10^2
b)
Intensity
6
8
10
12
14
16
18
20
22
24
2θ (degrees)

Figure 1

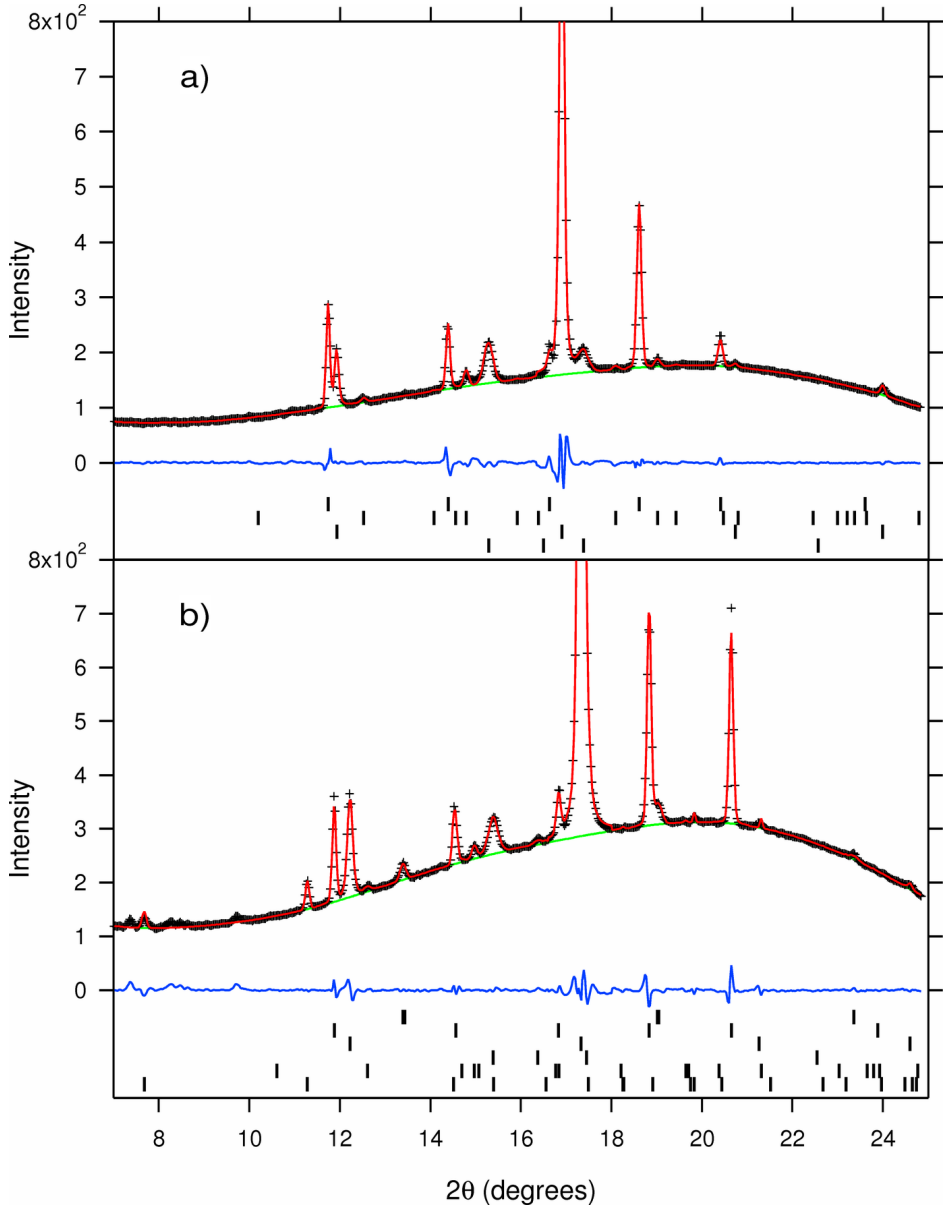
8x10^2
a)
Intensity
8x10^2
b)
Intensity
8
10
12
14
16
18
20
22
24
2θ (degrees)

Figure 2

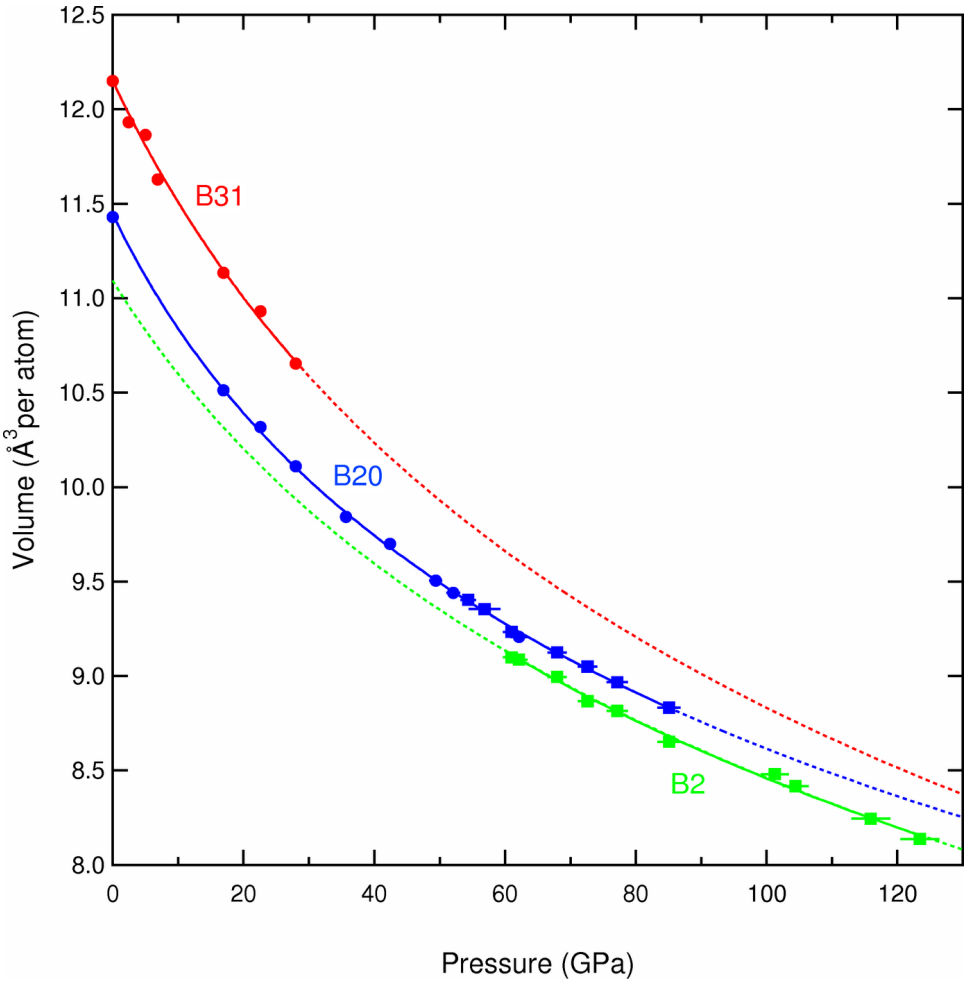
12.5
12.0
11.5
11.0
10.5
10.0
9.5
9.0
8.5
8.0
Volume (Å^3 per atom)
0
20
40
60
80
100
120
Pressure (GPa)
B31
B20
B2

Figure 3

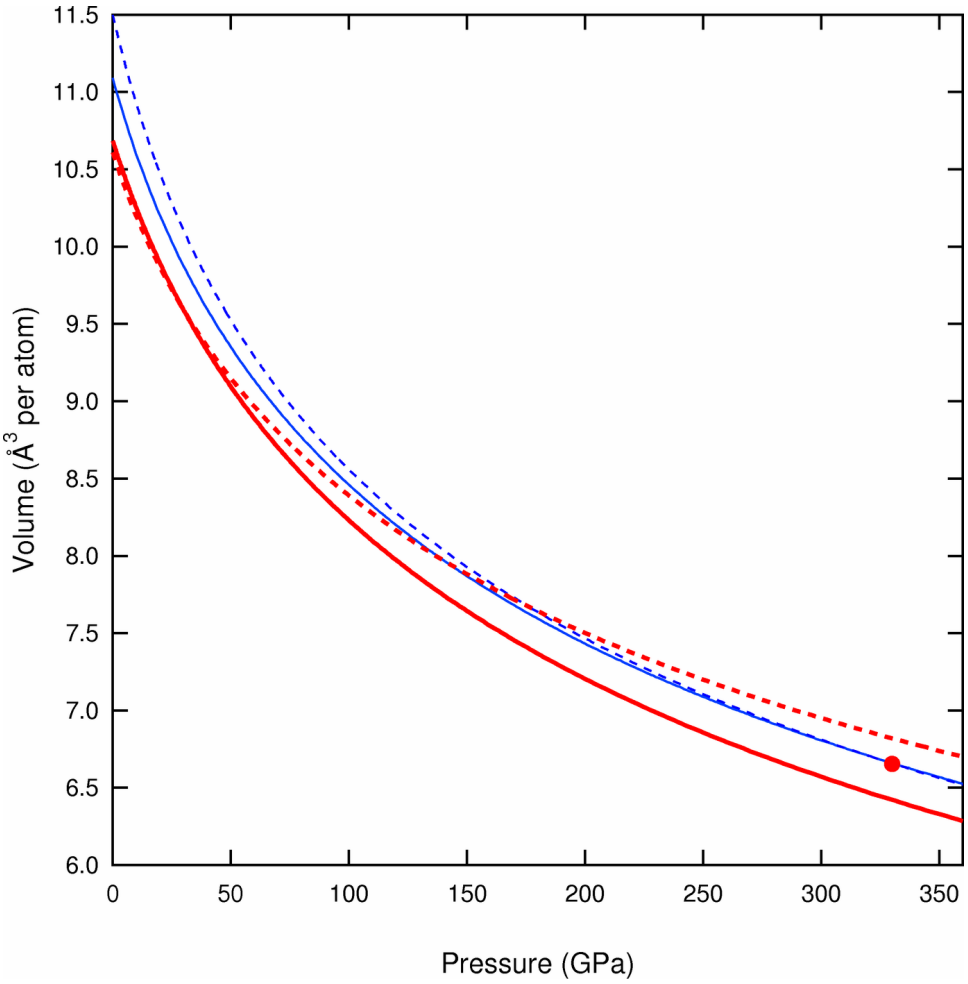
11.5
11.0
10.5
10.0
9.5
9.0
8.5
8.0
7.5
7.0
6.5
6.0
Volume (Å^3 per atom)
0
50
100
150
200
250
300
350
Pressure (GPa)

Figure 4

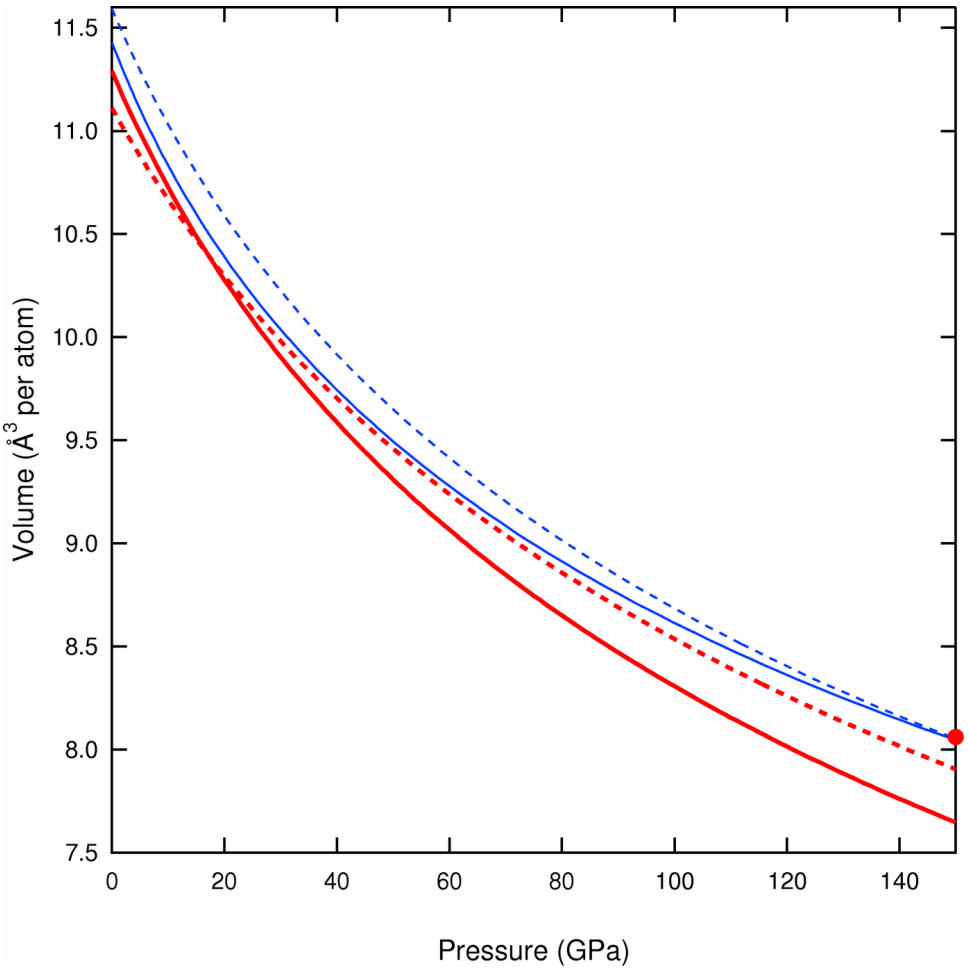
11.5
11.0
10.5
10.0
9.5
9.0
8.5
8.0
7.5
Volume (Å^3 per atom)
0
20
40
60
80
100
120
140
Pressure (GPa)

Figure 5